NANO · MICRO small
www.small-journal.com

Weak Dispersion of Exciton Landé Factor with Band Gap Energy in Lead Halide Perovskites: Approximate Compensation of the Electron and Hole Dependences

Natalia E. Kopteva, Dmitri R. Yakovlev, Erik Kirstein, Evgeny A. Zhukov, Dennis Kudlacik, Ina V. Kalitukha, Victor F. Sapega, Oleh Hordiichuk, Dmitry N. Dirin, Maksym V. Kovalenko, Andreas Baumann, Julian Höcker, Vladimir Dyakonov, Scott A. Crooker, and Manfred Bayer*

The optical properties of lead halide perovskite semiconductors in vicinity of the bandgap are controlled by excitons, so that investigation of their fundamental properties is of critical importance. The exciton Landé or *g*-factor g_X is the key parameter, determining the exciton Zeeman spin splitting in magnetic fields. The exciton, electron, and hole carrier *g*-factors provide information on the band structure, including its anisotropy, and the parameters contributing to the electron and hole effective masses. Here, g_X is measured by reflectivity in magnetic fields up to 60 T for lead halide perovskite crystals. The materials band gap energies at a liquid helium temperature vary widely across the visible spectral range from 1.520 up to 3.213 eV in hybrid organic–inorganic and fully inorganic perovskites with different cations and halogens: $FA_{0.9}Cs_{0.1}PbI_{2.8}Br_{0.2}$, $MAPbI_3$, $FAPbBr_3$, $CsPbBr_3$, and $MAPb(Br_{0.05}Cl_{0.95})_3$. The exciton *g*-factors are found to be nearly constant, ranging from +2.3 to +2.7. Thus, the strong dependences of the electron and hole *g*-factors on the bandgap roughly compensate each other when combining to the exciton *g*-factor. The same is true for the anisotropies of the carrier *g*-factors, resulting in a nearly isotropic exciton *g*-factor. The experimental data are compared favorably with model calculation results.

1. Introduction

Lead halide perovskite semiconductors attract currently great attention due to their exceptional electronic and optical properties, which make them highly promising for applications in photovoltaics, optoelectronics, radiation detectors, etc.[1–5] Their flexible chemical composition $APbX_3$, where the cation A can be cesium (Cs^+), methylammonium (MA^+), formamidinium (FA^+) and the anion X can be I^-, Br^-, Cl^-, offers huge tunability of the band gap from the infrared up to the ultraviolet spectral range.

The optical properties of perovskite semiconductors in the vicinity of the band gap are controlled by excitons, which are electron-hole pairs bound by the Coulomb interaction. The exciton binding energy ranges from 14 to 64 meV,[6,7] making them stable at room temperature at least for the large binding energies. In-depth studies of exciton properties, such as of their

N. E. Kopteva, D. R. Yakovlev, E. Kirstein, E. A. Zhukov, D. Kudlacik, M. Bayer
Experimentelle Physik 2
Technische Universität Dortmund
44227 Dortmund, Germany
E-mail: natalia.kopteva@tu-dortmund.de

I. V. Kalitukha, V. F. Sapega
Ioffe Institute
Russian Academy of Sciences
St. Petersburg 194021, Russia

The ORCID identification number(s) for the author(s) of this article can be found under https://doi.org/10.1002/smll.202300935

DOI: 10.1002/smll.202300935

O. Hordiichuk, D. N. Dirin, M. V. Kovalenko
Department of Chemistry and Applied Biosciences
Laboratory of Inorganic Chemistry
ETH Zürich, Zürich 8093, Switzerland

O. Hordiichuk, M. V. Kovalenko
Department of Advanced Materials and Surfaces
Laboratory for Thin Films and Photovoltaics
Empa–Swiss Federal Laboratories for Materials Science and Technology
Dübendorf 8600, Switzerland

A. Baumann, J. Höcker, V. Dyakonov
Experimental Physics VI
Julius-Maximilian University of Würzburg
97074 Würzburg, Germany

S. A. Crooker
National High Magnetic Field Laboratory
Los Alamos National Laboratory
Los Alamos, NM 87545, USA

energy and spin level structure or their relaxation dynamics, which disclose unifying trends for the whole class of lead halide perovskites, are therefore of key importance for basic and applied research.

The band structure of lead halide perovskites is inverted compared to conventional III-V and II-VI semiconductors. As a result, the strong spin-orbit interaction influences the conduction rather than the valence band. Spin physics provides high precision tools for addressing electronic states in the vicinity of the band gap: the Landé *g*-factors of electrons and holes are inherently linked via their values and anisotropies to the band parameters, which in turn determine the charge carrier effective masses.[8,9] On the other hand, the *g*-factors are the key parameters for the coupling of carrier spins to a magnetic field and thus govern spin-related phenomena and spintronics applications, a largely uncharted area for perovskites.

We recently showed experimentally and theoretically that a universal dependence of the electron and hole *g*-factors showing strong variations with the band gap energy can be established for the whole family of hybrid organic–inorganic and fully inorganic lead halide perovskite crystals.[10,11] These measurements were performed by time-resolved Kerr rotation and spin-flip Raman scattering spectroscopy including an analysis of the *g*-factor anisotropy. As the exciton *g*-factor g_X is contributed by the electron and the hole *g*-factor, one may expect a similarly universal dependence for g_X. As some *g*-factor renormalization due to the finite carrier *k*-vectors in the exciton is expected, a direct measurement of the free exciton Zeeman splitting, e.g., by magneto-reflectivity or magneto-absorption, provides valuable insight. The data published so far concern mostly polycrystalline materials with broad exciton lines, which diminish the accuracy of exciton *g*-factor evaluation.[6,7,12,13] Magneto-optical studies of high quality crystals are needed to that end, in combination with high magnetic fields providing large Zeeman splittings.[14–16]

In this study, we measured the exciton *g*-factors in lead halide perovskite crystals with different band gap energies using magneto-reflectivity in strong magnetic fields up to 60 T. We compare the experimental data with the electron and hole *g*-factors measured by time-resolved Kerr ellipticity and spin-flip Raman scattering. We find that the exciton *g*-factor is nearly independent of the band gap energy that varies from 1.5 to 3.2 eV through the choice of cations and/or halogens in the perovskite composition. This behavior is in good agreement with the results of model calculations. We also find that the anisotropies of the electron and hole *g*-factors compensate each other, such that the net exciton *g*-factor becomes isotropic.

2. Results

We studied five lead halide perovskite crystals with bandgap energies (E_g) covering basically the whole visible spectral range from 1.5 up to 3.2 eV. Details of the synthesis of these high-quality crystals are given in the Section S1 (Supporting Information). The hybrid organic–inorganic compounds $FA_{0.9}Cs_{0.1}PbI_{2.8}Br_{0.2}$ (E_g = 1.520 eV at the cryogenic temperature of $T = 1.6$ K) and $MAPbI_3$ ($E_g = 1.652$ eV) have band gap energies close to the near-infrared. Replacing the iodine halogen with bromine and chlorine results in a blue-shift of the band gap for $FAPbBr_3$ (2.216 eV) and $MAPb(Br_{0.05}Cl_{0.95})_3$ (3.213 eV). To develop a complete picture, we also study the fully inorganic perovskite $CsPbBr_3$ (2.359 eV).

2.1. Optical Properties

An overview of the optical properties of the studied crystals at the temperature of $T = 1.6$ K is given in **Figure 1**. We are interested in the properties of free excitons, which exhibit pronounced resonances in the reflectivity spectra of four studied crystals, but not for $FA_{0.9}Cs_{0.1}PbI_{2.8}Br_{0.2}$. For the latter, we measured the photoluminescence excitation (PLE) spectrum, where the pronounced peak at 1.506 eV corresponds to the exciton resonance energy, E_X. The exciton resonances are marked by the arrows in all panels and their energies are summarized in **Table 1**.

Photoluminescence (PL) spectra are also shown in Figure 1. At low temperature, the excitons are typically localized or bound to impurities, and the emission from free excitons is weak. It can be seen as a weak PL shoulder for $FA_{0.9}Cs_{0.1}PbI_{2.8}Br_{0.2}$ and $MAPbI_3$ only. The PL spectra are Stokes-shifted from the free exciton resonances and are composed of several lines, the origins of which are discussed in literature, but are not yet fully clarified.[18–21] The recombination dynamics, examples of which we show in Figure S1 (Supporting Information), are complex and show different characteristic time scales ranging from hundreds of picoseconds, as typical for free exciton lifetimes, up to tens of microseconds. The longer times are associated with resident electrons and holes, which are spatially separated due to localization at different sites. The dispersion in distances between an electron and a hole, resulting in different overlaps between their wave functions and trapping-detrapping processes, provide a strong variation of decay times. The coexistence of long-lived localized electrons and holes, which we refer to as resident carriers, is typical for lead halide perovskites, as confirmed by spin-dependent experimental techniques.[10,15,22,23]

2.2. Measurement of Exciton, Electron, and Hole *g*-Factors

The band gap in lead halide perovskite semiconductors is located at the *R*-point of the Brillouin zone for the cubic crystal lattice and at the Γ-point for the tetragonal or orthorhombic lattices.[24] In all these cases the states at the bottom of the conduction band and the top of the valence band have spin 1/2. In an external magnetic field *B*, the electron (hole) Zeeman splittings, $E_{Z,e(h)} = \mu_B g_{e(h)} B = \mu_{Be(h)} B$, are determined by the *g*-factors, g_e and g_h. Here μ_B is the Bohr magneton.

The bright (optically-active) exciton, composed of an electron and a hole, has angular momentum $L = \pm 1$. Its spin sublevels are split by the Zeeman energy $E_Z = \mu_B g_X B E_Z = \mu_B g_X B$ with the exciton *g*-factor g_X. In the Faraday geometry with the magnetic field parallel to the light wave vector ($\mathbf{B}_F \| \mathbf{k}$), the exciton states with opposite spin orientation can be distinguished by the circular polarization of the reflected light.

An example of such measurements for the $FAPbBr_3$ crystal is given in **Figure 2**a, where the reflectivity spectra detected in σ^+ or σ^- polarization at $B_F = 7$ T are shown. One clearly sees the Zeeman splitting of the exciton resonance with $E_Z = 1.09$ meV. The dependence of E_Z on B_F is a linear one, see Figure 2b. From

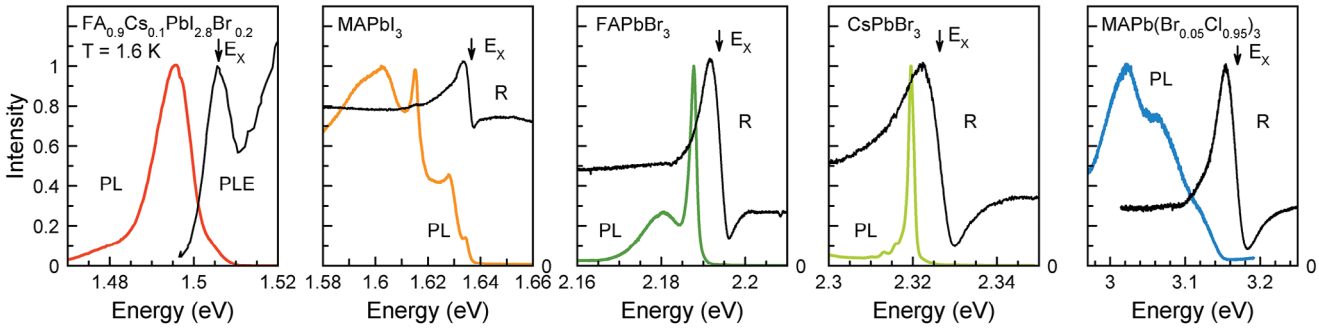

Figure 1. Optical properties of lead halide perovskite crystals with various band gaps at a temperature of 1.6 K. The colored lines show the photoluminescence spectra for continuous wave excitation at $E_{exc} = 3.06$ eV, using the laser power density of 5 mW/cm^2. For $MAPb(Br_{0.05}Cl_{0.95})_3$ the excitation energy is $E_{exc} = 3.23$ eV. The black lines show the PLE spectrum for $FA_{0.9}Cs_{0.1}PbI_{2.8}Br_{0.2}$ and the reflectivity spectra for the other samples.

the slope we evaluate the exciton *g*-factor $g_{F,X} = +2.7$. Note that in this experiment the *g*-factor sign can be determined: positive values correspond to a high (low) energy shift of the σ^+ (σ^-) polarized resonance. We performed similar magneto-reflectivity experiments for $MAPbI_3$, $CsPbBr_3$, and $MAPb(Br_{0.05}Cl_{0.95})_3$ and the measured exciton *g*-factors ($g_{F,X}$) are given in Table 1. The dependences of E_Z on B_F for $MAPbI_3$ and $MAPb(Br_{0.05}Cl_{0.95})_3$ are shown in Figure S2 (Supporting Information) and for $CsPbBr_3$ in **Figure 3**b.

The Zeeman splitting of the bright exciton is given by the sum of the electron and hole Zeeman splittings, so that

$$g_X = g_e + g_h \quad (1)$$

To what extent this equation is exactly fulfilled, needs to be checked specifically for each material, as some renormalization of the exciton *g*-factor may take place when the carriers are bound to form an exciton, in which they both are in motion. The renormalization could be caused by band mixing at finite wave vectors. We show below that Equation (1) is reasonably well fulfilled for the studied materials.

Time-resolved Kerr rotation and Kerr ellipticity are powerful techniques for measuring directly the carrier *g*-factors by analyzing the Larmor precession frequencies, ω_L, of their spins.[25] In lead halide perovskites, resident electrons and holes coexist at low temperatures, so that their *g*-factors can be measured in one sample in a single experiment.[10,15,22,23,26,27] We perform measurements of the time-resolved Kerr ellipticity (TRKE) on the $FAPbBr_3$ crystal, with the pump and probe laser energy tuned to the exciton resonance. The TRKE dynamics measured in the Voigt geometry with the magnetic field perpendicular to the light wave vector ($\mathbf{B}_V \perp \mathbf{k}$, $B_V = 0.5$ T) are shown in Figure 2c by the blue line. It contains two Larmor precession frequencies, which we decompose by the fit function given in the Experimental Section. We plot the electron and hole contributions separately in the same figure. Based on the established universal dependence of the carrier *g*-factors on the bandgap energy in lead halide perovskites,[10] we assign the higher Larmor frequency to the electrons and the smaller frequency to the holes. Their *g*-factors of $g_{V,e} = +2.44$ and $g_{V,h} = +0.41$ are evaluated with high accuracy from the magnetic field dependence of the Zeeman splitting $E_{Z,e(h)} = \hbar\omega_{L,e(h)}$ (Figure 2d), where $\hbar$ is the reduced Planck constant, using $|g_{e(h)}| = \hbar\omega_{L,e(h)}/(\mu_B B)$.

The sign of the *g*-factor cannot be determined directly from the TRKE dynamics in the Voigt geometry. However, dynamic nuclear polarization in tilted magnetic field[22] and theoretical calculation of the carrier *g*-factors' universal dependence[10] allow us to identify it as positive for both electrons and holes in $FAPbBr_3$.

We measure the anisotropy of the electron and hole *g*-factors in $FAPbBr_3$ by rotating the magnetic field using a vector

Table 1. Parameters of lead halide perovskite crystals at cryogenic temperatures of 1.6 – 10 K.

Material	E_g (eV)	E_X (eV)	E_B (meV)	m_X (m_0)	$g_{V,e}$[10]	$g_{V,h}$[10]	$g_{V,e} + g_{V,h}$	$g_{F,e}$[10]	$g_{F,h}$[10]	$g_{F,e} + g_{F,h}$	$g_{F,X}$
$FA_{0.9}Cs_{0.1}PbI_{2.8}Br_{0.2}$ [a]	1.520	1.506	14[6]	0.09[6]	+3.48	-1.15	+2.33	+3.60	-1.22	+2.38	-
$MAPbI_3$ [b]	1.652	1.636	16[6]	0.104[6]	+2.81	-0.68	+2.13	+2.57	-0.34	+2.23	+2.3
$MAPbI_3$[14]	1.656	1.640	16[6]	0.104[6]	–	–	–	–	–	–	2.66 ± 0.1[d]
$FAPbBr_3$	2.216	2.194	22[6]	0.115[6]	+2.44	+0.41	+2.85	+2.32	+0.36	+2.68	+2.7
$MAPbBr_3$[16]	2.275	2.250	25[7]	0.117[7]	–	–	–	–	–	–	2.6[d]
$CsPbBr_3$	2.359	2.326	33[17]	0.126[17]	+1.69	+0.85	+2.54	+2.06	+0.65	+2.71	+2.35
$MAPb(Br_{0.05}Cl_{0.95})_3$	3.213	3.168	45[c]	–	–	+1.33	–	–	–	–	+2.5

[a] In Ref. [6] the exciton effective mass m_X and the exciton binding energy E_B are given for $FAPbI_3$. We consider that their values for $FA_{0.9}Cs_{0.1}PbI_{2.8}Br_{0.2}$ are very close; [b] $MAPbI_3$ shows a complex anisotropy of the electron and hole *g*-factors.[10] Here, the given values of g_V correspond to $\theta = 60°$ and g_F to $\theta = 150°$; [c] The value is obtained from a linear approximation of the dependence of the exciton binding energy E_B on E_g. m_X is the exciton effective mass; [d] In the original papers, the sign of the *g*-factor was not given.

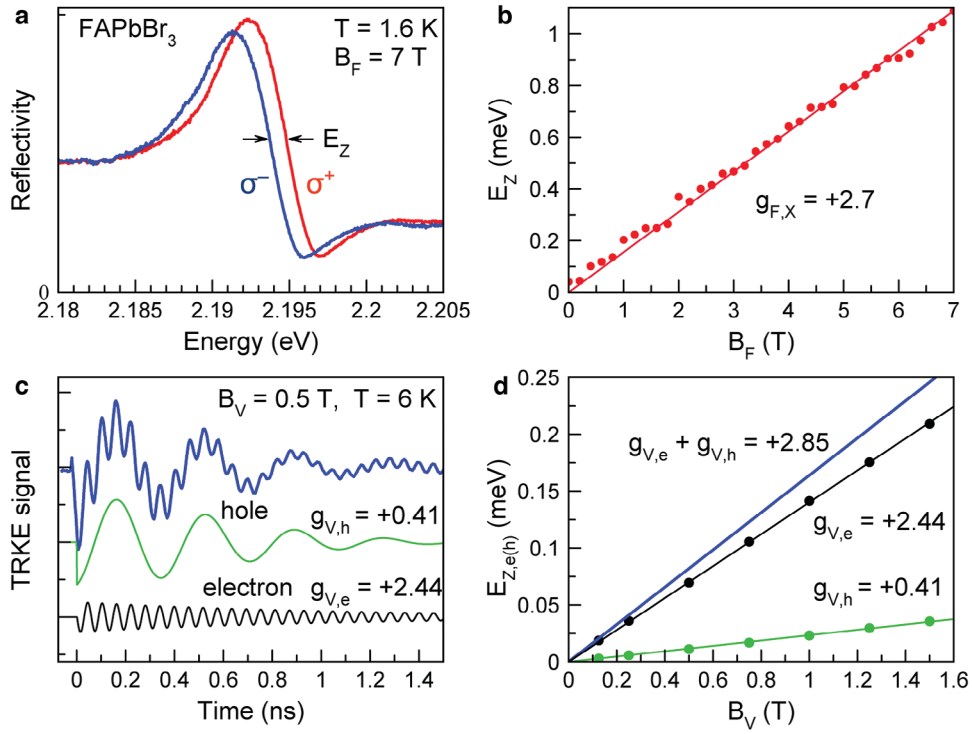

Figure 2. Magneto-optical properties of excitons, as well as resident electrons and holes in a $FAPbBr_3$ crystal. a) Reflectivity spectra measured in σ^+ (red line) and σ^- (blue line) polarization in the longitudinal magnetic field $B_F = 7$ T at $T = 1.6$ K. b) Exciton Zeeman splitting as function of B_F measured in magneto-reflectivity. Slope of the linear fit gives $g_{F,X} = +2.7$. c) Time-resolved Kerr ellipticity signal (blue) measured at $B_V = 0.5$ T, $T = 6$ K, using the laser photon energy of 2.188 eV. The electron (black) and hole (green) components are obtained from decomposing the signal. d) Dependence of the Zeeman splitting of the hole (green), the electron (black), and their sum (blue) on B_V.

magnet, see the Figure S3 (Supporting Information). The *g*-factor anisotropy is small, namely the *g*-factors in the Faraday geometry ($g_{F,e} = +2.32$ and $g_{F,h} = +0.36$) are close to the ones in the Voigt geometry ($g_{V,e} = +2.44$ and $g_{V,h} = +0.41$). This is typical for lead halide perovskites with an FA cation, as in these materials the structural tolerance factor is close to unity and structural modifications at low temperatures are weak. Also for $FA_{0.9}Cs_{0.1}PbI_{2.8}Br_{0.2}$, we earlier reported nearly isotropic electron and hole *g*-factors.[22]

The sum of the carrier *g*-factors $g_{F,e} + g_{F,h} = +2.68$ in $FAPbBr_3$ coincides closely with the exciton *g*-factor $g_{F,X} = +2.7$ obtained from magneto-reflectivity measurements. These values are also close for $MAPbI_3$ ($g_{F,e} + g_{F,h} = +2.23$ and $g_{F,X} = +2.3$) and furthermore are not differ much in $CsPbBr_3$ ($g_{F,e} + g_{F,h} = +2.71$ and $g_{F,X} = +2.35$), see Table 1. Note that the experimental accuracy of *g*-factor values received from magneto-reflectivity is ±0.1 and from the TRKE is ±0.05.

2.3. Anisotropy of Exciton *g*--Factor

In $CsPbBr_3$ crystals, the anisotropy of the electron and hole *g*-factors is pronounced. The results measured by spin-flip Raman scattering (SFRS), for details see the Figure S4 (Supporting Information), are shown in Figure 3a. Here θ is the angle of the magnetic field tilt from the Faraday ($\theta = 0°$) to the Voigt ($\theta = 90°$) geometry. In this experiment, the c-axis is oriented perpendicular to the light *k*-vector, so that $\mathbf{B} \| c$ corresponds to the Voigt geometry. Note, that contrary to TRKE, spin-flip lines are detectable also in the Faraday geometry and, therefore, $g_{F,e(h)}$ are measured directly. The g_e and g_h dependences on θ are described by

$$g_{e(h)}(\theta) = \sqrt{g_{F,e(h)}^2 \cos^2\theta + g_{V,e(h)}^2 \sin^2\theta} \quad (2)$$

The electron and hole *g*-factors are both positive in $CsPbBr_3$, but their anisotropies are orthogonal to each other. The electron *g*-factor is largest in the Faraday geometry ($g_{F,e} = +2.06$) and decreases in the Voigt geometry to $g_{V,e} = +1.69$, while the hole *g*-factor increases from the Faraday toward the Voigt geometry from $g_{F,h} = +0.65$ up to $g_{V,-h} = +0.85$. Interestingly, the sum of the carrier *g*-factors changes only weakly from +2.71 to +2.54, see the blue crosses in Figure 3a, demonstrating that the exciton *g*-factor anisotropy is weak. Note, that the exciton spin flip is also visible as a weak line in SFRS spectra (Figure S4, Supporting Information). Its g-factor, shown in Figure 3a by red circles, coincides very well with the blue crosses data. The weak anisotropy of the exciton *g*-factor is a common feature for the lead halide perovskites, as confirmed by the data for $MAPbI_3$, where the strong anisotropies of the electron and hole *g*-factors nearly compensate each other in their sum, see Table 1.

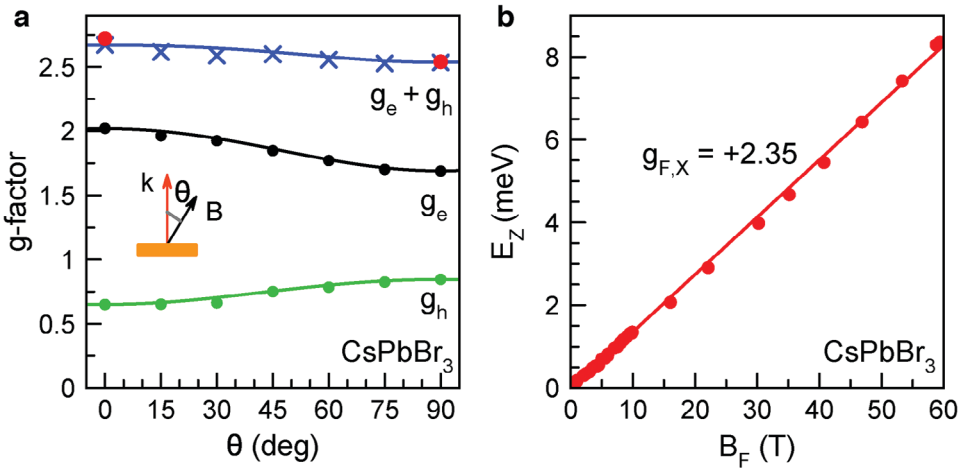

Figure 3. a) Anisotropy of the electron (black circles) and hole (green circles) *g*-factors measured by SFRS for $CsPbBr_3$. $B = 5$ T and $T = 1.6$ K. Red circles present the exciton *g*-factor. The black and green lines are calculated with Equation (2), using the parameters from Table 1. The blue crosses are experimental data of $g_e + g_h$, the blue line is the sum of the fits shown by the black and green lines. b) Magnetic field dependence of the exciton Zeeman splitting measured from magneto-reflectivity in the Faraday geometry for $CsPbBr_3$. $T = 1.6$ K. The symbols are experimental data and the line is a linear fit.

2.4. Exciton Zeeman Splitting in Strong Pulsed Magnetic Fields

We examined the exciton Zeeman splitting in the $CsPbBr_3$ crystal in very strong magnetic fields up to 60 T, using a pulsed magnet at the National High Magnetic Field Laboratory in Los Alamos. The experiments were motivated by the possibility to reach large Zeeman splittings, thus improving the accuracy of the exciton *g*-factor evaluation, and also by searching for a possible nonlinearity of the Zeeman splitting by field-induced band mixing. Magneto-reflectivity was measured at $T = 1.6$ K and the Zeeman splitting of the oppositely circularly polarized exciton resonances (similar as in Figure 2a) was assessed. The results are shown in Figure 3b. The exciton Zeeman splitting increases linearly with magnetic field over the whole range up to 60 T. The evaluated $g_{F,X} = +2.35$. The high linearity indicates that band mixing is negligibly small in lead halide perovskites even in very strong magnetic fields. This is explained by the simple spin structure (spin 1/2) of the electronic states in the vicinity of the bandgap, which contribute to the exciton wave function. The shift of the higher-lying electron states with momentum 3/2 due to the spin-orbit splitting in the conduction band is about 1.5 eV, which is large enough to exclude a significant admixture of these states to the ground exciton state by the magnetic field. Note that in this respect the lead halide perovskites principally differ from conventional III-V and II-VI semiconductors, for which strongly nonlinear Zeeman splittings were reported in GaAs- and CdTe-based quantum wells.[28,29]

2.5. Band Gap Dependence of Exciton *g*-Factor

To summarize the information on the exciton *g*-factors for the whole class of lead halide perovskites and highlight general trends, we show in **Figure 4** the experimental data collected in Table 1 as function of the band gap energy. Our data for $g_{F,X}$ measured by magneto-reflectivity are shown by the closed red circles. We combine them with literature data (open red circles), also measured by magneto-reflectivity on $MAPbI_3$ and $MAPbBr_3$ crystals.[14,16] One can see that the exciton *g*-factor is nearly independent of the band gap energy varying from 1.5 to 3.2 eV. The exciton *g*-factors change only in a small range from +2.3 to +2.7. Compared to the average, this corresponds to a variation well below 10%, while the electron *g*-factor varies by significantly more than 50%.

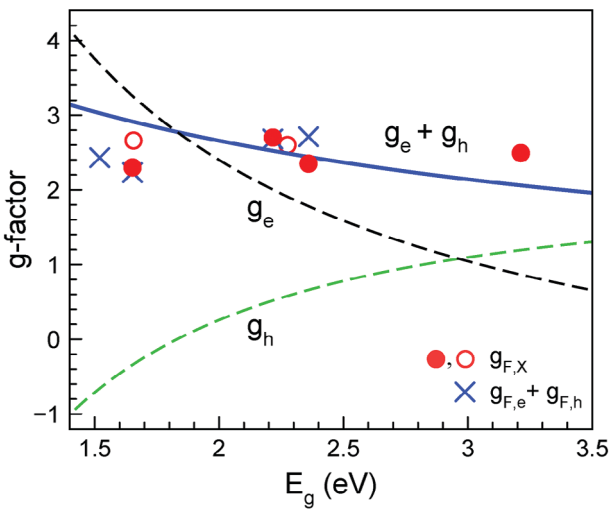

Figure 4. Dependence of the exciton *g*-factor measured by magneto-reflectivity (closed red circles are our data and open red circles are from Refs. [14, 16]) and of the sum of carrier *g*-factors evaluated from TRKE and SFRS (crosses) on the band gap energy. The data are taken at cryogenic temperatures of 1.6 – 10 K. The dashed lines are model calculations[10] with Equations (3) and (4) for the hole (green) and the electron (black) *g*-factors, which closely match the experimental data given in Table 1. The blue line is the sum of their contributions calculated with Equation (5). Size of the symbols includes the error.

We show in Figure 4 also the sum values of $g_{F,e} + g_{F,h}$ by the crosses, which follow closely the $g_{F,X}$ values. Therefore, we conclude that the renormalization of the carrier *g*-factors in the excitons is small in the lead halide perovskites.

Let us compare our experimental data with model predictions. We showed recently experimentally and theoretically that the electron and hole *g*-factors in the lead halide perovskites follow universal dependences on the band gap energy.[10] According calculations are given in Figure 4 by the dashed lines. They account for the fact that in the vicinity of the band gap the band structure of hybrid organic–inorganic and of fully inorganic lead halide perovskites is strongly contributed by Pb orbitals. Then, for the holes in the valence band, the main contribution to the *g*-factor is due to $\mathbf{k} \cdot \mathbf{p}$ mixing with the conduction band. For the cubic phase it is described by Ref. [10, 30]:

$$g_h = 2 - \frac{4}{3}\frac{p^2}{m_0}\left(\frac{1}{E_g} - \frac{1}{E_g + \Delta}\right) \quad (3)$$

Here, p is the interband matrix element of the momentum operator, $\Delta = 1.5$ eV is the spin-orbit splitting of the conduction band, m_0 is the electron effective mass, and $\hbar p/m_0 = 6.8$ eVÅ. For electrons, the $\mathbf{k} \cdot \mathbf{p}$ mixing with the top valence band and the remote valence states are important:

$$g_e = -\frac{2}{3} + \frac{4}{3}\frac{p^2}{m_0 E_g} + \Delta g_e. \quad (4)$$

Here, $\Delta g_e = -1$ is the remote band contribution evaluated as fitting parameter in Ref. [10]. One clearly sees that both electron and hole *g*-factors change strongly with increasing E_g.

Using Equations (3) and (4) we obtain for the sum of the electron and hole *g*-factors:

$$g_e + g_h = \frac{4}{3} + \frac{4}{3}\frac{p^2}{m_0}\frac{1}{E_g + \Delta} + \Delta g_e \quad (5)$$

It is shown by the solid blue line in Figure 4. One can see that it has much weaker dependence on the bandg ap compared to the *g*-factors of the individual carriers. The calculated dependence for $g_e + g_h$ is in good agreement with the experimental data on both $g_{F,X}$ and $g_e + g_h$ shown in Figure 4. Note that the similar cancellation is valid for the angle dependence of the exciton *g*-factor, shown forexample for $CsPbBr_3$ in Figure 3a. The related formalism has been developed in Ref. [10], and we give its key equations in Section S6 (Supporting Information).

The observed, approximate independence of the exciton *g*-factor on the band gap E_g is a consequence of the underlying simple band structure, determined by the lowest conduction band *c*, $\pm 1/2$ and the highest valence band *v*, $\pm 1/2$, showing both only a twofold spin degeneracy. As shown above,[10] the contributions to the individual *g*-factors from the $\mathbf{k} \cdot \mathbf{p}$ mixing of these bands proportional to $1/E_g$ cancel each other in the exciton *g*-factor. This is in striking contrast to the Zeeman splitting of the exciton sublevels in conventional III-V or II-VI bulk semiconductors of cubic symmetry, like GaAs or CdTe. First, in these well-studied semiconducting materials, the conduction band Γ_6 is simple, but the electron *g*-factor is strongly dependent not only on E_g, but also on the spin-orbit splitting Δ of the valence band Γ_8, the latter varying in a wide range.[31] Second and more importantly, the hole is characterized by the effective angular momentum $j = 3/2$ so that it is fourfold degenerate. The valence band degeneracy leads to complicated exciton level splitting and structure of its wave function as result of the interplay of heavy hole-light hole mixing and electron-hole exchange interaction.[32–34] Even if the field-induced hole mixing and the exchange interaction in the exciton are disregarded, the effective *g*-factor of the bright exciton (A-exciton) contains $1/E_g$ contributions.

While the mixing of the bands forming the gap cancels thus in g_X, the mixing of the valence band with the higher lying, remote conduction band still contributes, but here the variation with E_g is damped by adding the spin-orbit splitting which is comparatively large in the perovskites. The situation is similar to the one in transition metal dichalcogenide monolayers, where the bright exciton *g*-factor is as well largely determined by the remote bands, while the mutual contributions of the valence band to the electron *g*-factor and of the conduction band to the hole *g*-factor cancel out in the exciton *g*-factor.[35–37]

Up to now we discussed the bandgap dependence of the bright exciton *g*-factor, $g_X = g_e + g_h$. For the optically-forbidden dark exciton the *g*-factor value is given by the difference $g_e - g_h$. Due to the opposite variation of the electron and hole *g*-factors, the dependence on E_g is expected to be even stronger for the dark exciton than for individual electron and hole, see Figure S5 (Supporting Information). Also a stronger anisotropy for the dark exciton *g*-factor, compared to the bright exciton *g*-factor which is nearly isotropic, is expected.

To summarize, the exciton *g*-factors in hybrid organic–inorganic and fully inorganic lead halide perovskites have positive signs and show relatively constant values over a large range of band gap energies. Further, they are nearly isotropic. It turns out that the strong band gap dependences and anisotropies of the individual electron and hole *g*-factors contributing to the exciton largely compensate each other. It would be important to extend these studies to perovskite semiconductors based on another metal ions, e.g., lead-free Sn-based materials. Also the role of quantum confinement for carriers and excitons in perovskite nanocrystals and 2D materials would be interesting to examine.

3. Experimental Section

Samples: The class of lead halide perovskites possesses the composition $APbX_3$, where the *A*-cation was typically Cs^+, methylammonium (MA^+, $CH_3NH_3^+$), or formamidinium (FA^+, $CH(NH_2)_2^+$), and the *X*-anion was one of the halogens Cl^-, Br^-, or I^-. The ratio of the anion to cation ion radii defines the Goldschmidt tolerance factor *t*. If it was close to unity,[38] then the structure could be synthesized. Replacing the anion leads to a change in the bandgap width from the infrared to the ultraviolet spectral range. This study used single lead halide perovskite crystals with different bandgap widths grown out of solution with the inverse temperature crystallization (ITC) technique.[5,39,40] For specific crystals the ITC protocols were modified, and for the five crystals studied here ($FA_{0.9}Cs_{0.1}PbI_{2.8}Br_{0.2}$, $MAPbI_3$, $FAPbBr_3$, $CsPbBr_3$, and $MAPb(Br_{0.05}Cl_{0.95})_3$) details of their synthesis are given in Section S1 (Supporting Information) and in Ref. [10].

Magneto-Reflectivity: The samples were placed in a cryostat and immersed in either superfluid liquid helium at $T = 1.6$ K or in - helium gas for $T = 6 - 10$ K. For experiments in *dc* magnetic fields, two cryostats equipped with a split-coil superconducting magnet were used. One with a single split

coil produces magnetic fields up to 10 T in one direction. Another was a vector magnet with three orthogonally oriented split coils,which allows to apply and rotate the magnetic field (up to 3 T) in any direction.

A halogen lamp was used for measuring magneto-reflectivity. The light wave vector, **k**, was perpendicular to the sample surface and the reflectivity was measured in backscattering geometry. The signal was analyzed for σ^+ and σ^- circular polarization and recorded after dispersion with an 0.5-meter spectrometer with a Silicon charge-coupled-device camera. The external magnetic field was applied parallel to the light *k*-vector, $\mathbf{B}_F \| \mathbf{k}$ (Faraday geometry). In the TRKE and SFRS experiments, the Voigt geometry was used ($\mathbf{B}_V \perp \mathbf{k}$), as well as tilted geometries between Faraday and Voigt. Here, the tilt angle θ is defined as the angle between $\mathbf{B}_F$ and $\mathbf{B}_V$, where $\theta = 0^\circ$ corresponds to the Faraday geometry. Experiments in pulsed magnetic fields up to 60 T were performed in the Faraday geometry, following previously-described methods.[41]

Time-Resolved Kerr Ellipticity (TRKE): The coherent spin dynamics were studied by a pump-probe method. Pump and probe light, emitted from a pulsed titanium-sapphire (Ti:Sa) laser,[25] had the same photon energy. Both pulses had duration of 1.5 ps with a spectral width of about 1 nm (1.5 meV). Laser repetition rate was 76 MHz, which corresponds to repetition period $T_R = 13.2$ ns. An optical parametric oscillator (OPO) with internal frequency doubling was used to convert the photon energy of the Ti:Sa laser so that it could be resonantly tuned to the exciton resonance in $FAPbBr_3$.

The pump pulses went through a mechanical delay line and were time-delayed with respect to the probe pulses. Pump helicity was modulated between σ^+ and σ^- circular polarization at the frequency of 50 kHz by a photo-elastic modulator (PEM). Probe polarization was linear, but the amplitude was modulated at the frequency of 84 kHz by PEM. The polarization of the reflected probe beam was analyzed via balanced photodiodes and a lock-in amplifier (Kerr signal). The signal of all perovskite samples was elliptically polarized, therefore Kerr ellipticity signal was measured. Kerr ellipticity signal oscillates and decays in time in transverse magnetic field, due to the Larmor precession and spin relaxation. In case of perovskites, both electrons and holes spin coherence were observed in the Kerr ellipticity signal. It can be described as a sum of two decaying cosine functions: $A_{KE} = S_e \cos(\omega_{L,e} t) \exp(-t/T^*_{2,e}) + S_h \cos(\omega_{L,h} t) \exp(-t/T^*_{2,h})$. Here, $S_{e(h)}$ are the electron and hole spin polarization right after pump action. $T^*_{2,e(h)}$ are the carrier spin dephasing times. The Larmor precession frequencies $\omega_{L,\,e(h)}$ is recalculated to *g*-factors with $|g_{e(h)}| = \hbar\omega_{L,\,e(h)}/(\mu_B B)$. TRKE signal do not provide information about *g*-factor sign. The sign of the carrier *g*-factors could be identified in tilted magnetic field geometry through the dynamic nuclear polarization effect, for details see Refs. [22, 23].

Spin-Flip Raman Scattering (SFRS): The Zeeman splitting of resident carriers spin sublevels could be detected directly by the SFRS technique. The light scattered from the sample had the spectral shift (or Raman shift) from the laser photon energy,[42] due to the phonon assisted spin-flip of carriers. For the semiconductors, Raman shift is about 1 meV at magnetic field of 10 T. The experiments were performed for the $CsPbBr_3$ sample immersed in superfluid liquid helium ($T = 1.6$ K). The SFRS signal was excited by laser with photon energy of 2.330 eV at exciton resonance, with the laser power density of 1 Wcm^{-2}. The SFRS signal was measured in the backscattering geometry. A Jobin-Yvon U1000 double monochromator with one meter focal length was used for obtaining the SFRS spectra with high resolution of 0.2 cm^{-1} (0.024 meV). The signal was detected by a cooled GaAs photomultiplier and conventional photon counting electronics. The spectrally narrow laser, high spectral resolution of the spectrometer and efficient suppression of the scattered laser light allowed to detect Raman shifts from 0.1 to 3 meV. The SFRS spectra were measured for cross-polarized (σ^-/σ^+) circular polarizations of excitation (σ^-) and detection (σ^+).

Supporting Information

Supporting Information is available from the Wiley Online Library or from the author.

Acknowledgements

The authors are thankful to M. M. Glazov, M. O. Nestoklon and E. L. Ivchenko for fruitful discussions. The authors acknowledged financial support by the Deutsche Forschungsgemeinschaft via the SPP2196 Priority Program (Project YA 65/26-1) and the International Collaborative Research Centre TRR160 (Projects A1 and B2). I.V.K. acknowledged support of the Russian Foundation for Basic Research (Project No. 19-52-12064). The work at ETH Zürich (D.N.D. and M.V.K.) was financially supported by the Swiss National Science Foundation (grant agreement 186406, funded in conjunction with SPP219 through DFG-SNSF bilateral program) and by ETH Zürich through ETH+ Project SynMatLab. J.H., A.B., and V.D. acknowledged financial support from the Deutsche Forschungsgemeinschaft through the Würzburg-Dresden Cluster of Excellence on Complexity and Topology in Quantum Matter-ct.qmat (EXC 2147, project-id 39085490), DY18/19-1 and from the Bavarian State Ministry of Education and Culture, Science and Arts within the Collaborative Research Network "Solar Technologies go Hybrid". Experiments at the National High Magnetic Field Laboratory were supported by the National Science Foundation DMR-1644779, the State of Florida, and the US Department of Energy.

Open access funding enabled and organized by Projekt DEAL.

Conflict of Interest

The authors declare no conflict of interest.

Data Availability Statement

The data that support the findings of this study are available from the corresponding author upon reasonable request.

Keywords

electron *g*-factor, exciton Landé factor, hole *g*-factor, lead halide perovskites, magneto-reflectivity, pump-probe Kerr ellipticity, spin-flip Raman scattering

Received: February 2, 2023
Revised: October 25, 2023
Published online:

[1] (Eds.: Z. V. Vardeny, M. C. Beard), *Hybrid Organic Inorganic Perovskites: Physical Properties and Applications*, World Scientific, Singapore **2022**.
[2] (Eds.: A. Vinattieri, G. Giorgi), *Halide Perovskites for Photonics*, AIP Publishing, Melville, New York, **2021**.
[3] Best Research - Cell Efficiency Chart, https://www.nrel.gov/pv/cell-efficiency.html, **2021**.
[4] A. K. Jena, A. Kulkarni, T. Miyasaka, *Chem. Rev.* **2019**, *5*, 3036.
[5] O. Nazarenko, S. Yakunin, V. Morad, I. Cherniukh, M. V. Kovalenko, *NPG Asia Mater.* **2017**, *9*, e373.
[6] K. Galkowski, A. Mitioglu, A. Miyata, P. Plochocka, O. Portugall, G. E. Eperon, J. T.-W. Wang, T. Stergiopoulos, S. D. Stranks, H. J. Snaith, R. J. Nicholas, *Energy Environ. Sci.* **2016**, *9*, 962.
[7] M. Baranowski, P. Plochocka, R. Su, L. Legrand, T. Barisien, F. Bernardot, Q. Xiong, C. Testelin, M. Chamarro, *Photon. Res.* **2020**, *8*, A50.
[8] E. L. Ivchenko, *Optical Spectroscopy of Semiconductor Nanostructures*, Alpha Science Int. , Harrow, UK **2005**.
[9] Z. G. Yu, *Scientific reports* **2016**, *6*, 28576.

[10] E. Kirstein, D. R. Yakovlev, M. M. Glazov, E. A. Zhukov, D. Kudlacik, I. V. Kalitukha, V. F. Sapega, G. S. Dimitriev, M. A. Semina, M. O. Nestoklon, E. L. Ivchenko, N. E. Kopteva, D. N. Dirin, O. Nazarenko, M. V. Kovalenko, A. Baumann, J. Höcker, V. Dyakonov, M. Bayer, *Nat. Commun.* **2022**, *13*, 3062.
[11] U. N. Huynh, Y. Liu, A. Chanana, D. R. Khanal, P. C. Sarcel, J. Huang, Z. V. Vardeny, *Nat. Commun.* **2022**, *13*, 1428.
[12] M. Hirasawa, T. Ishihara, T. Goto, K. Uchida, N. Miura, *Physica B* **1994**, *201*, 427.
[13] K. Tanaka, T. Takahashi, T. Ban, T. Kondo, K. Uchida, N. Miura, *Solid State Commun.* **2003**, *127*, 619.
[14] Z. Yang, A. Surrente, K. Galkowski, N. Bruyant, D. K. Maude, A. A. Haghighirad, H. J. Snaith, P. Plochocka, R. J. Nicholas, *J. Phys. Chem. Lett.* **2017**, *8*, 1851.
[15] V. V. Belykh, D. R. Yakovlev, M. M. Glazov, P. S. Grigoryev, M. Hussain, J. Rautert, D. N. Dirin, M. V. Kovalenko, M. Bayer, *Nat. Commun.* **2019**, *10*, 673.
[16] M. Baranowski, K. Galkowski, A. Surrente, J. Urban, Ł. Kłopotowski, S. Maćkowski, D. K. Maude, R. Ben Aich, K. Boujdaria, M. Chamarro, C. Testelin, P. K. Nayak, M. Dollmann, H. J. Snaith, R. J. Nicholas, P. Plochocka, *Nano Lett.* **2019**, *19*, 7054.
[17] Z. Yang, A. Surrente, K. Galkowski, A. Miyata, O. Portugall, R. J. Sutton, A. A. Haghighirad, H. J. Snaith, D. K. Maude, P. Plochocka, R. J. Nicholas, *ACS Energy Lett.* **2017**, *2*, 1621.
[18] V. S. Chirvony, J. P. Martínez-Pastor, *J. Phys. Chem. Lett.* **2018**, *9*, 4955.
[19] D. W. deQuilettes, K. Frohna, D. Emin, T. Kirchartz, V. Bulovic, D. S. Ginger, S. D. Stranks, *Chem. Rev.* **2019**, *119*, 11007.
[20] A. Bercegol, F. J. Ramos, A. Rebai, T. Guillemot, D. Ory, J. Rousset, V. Lombez, *J. Phys. Chem. C* **2018**, *122*, 24570.
[21] S. Kahmann, H. Duim, H.-H. Fang, M. Dyksik, S. Adjokatse, M. Rivera Medina, M. Pitaro, P. Plochocka, M. A. Loi, *Adv. Funct. Mater.* **2021**, *31*, 2103778.
[22] E. Kirstein, D. R. Yakovlev, M. M. Glazov, E. Evers, E. A. Zhukov, V. V. Belykh, N. E. Kopteva, D. Kudlacik, O. Nazarenko, D. N. Dirin, M. V. Kovalenko, M. Bayer, *Advanced Materials* **2022**, *34*, 2105263.
[23] E. Kirstein, D. R. Yakovlev, E. A. Zhukov, J. Höcker, V. Dyakonov, M. Bayer, *ACS Photonics* **2022**, *9*, 1375.
[24] J. Even, L. Pedesseau, C. Katan, M. Kepenekian, J.-S. Lauret, D. Sapori, E. Deleporte, *J. Phys. Chem.* **2015**, *119*, 10161.
[25] D. R. Yakovlev, M. Bayer, in *Spin Physics in Semiconductors*, (Ed.: M. I. Dyakonov), Springer International Publishing AG, New York **2017**, pp. 155–206.
[26] P. Odenthal, W. Talmadge, N. Gundlach, R. Wang, C. Zhang, D. Sun, Z.-G. Yu, Z. V. Vardeny, Y. S. Li, *Nature Physics* **2017**, *13*, 894.
[27] G. Garcia-Arellano, G. Trippé-Allard, L. Legrand, T. Barisien, D. Garrot, E. Deleporte, F. Bernardot, C. Testelin, M. Chamarro, *J. Phys. Chem. Lett.* **2021**, *12*, 8272.
[28] N. J. Traynor, R. J. Warburton, M. J. Snelling, R. T. Harley, *Phys. Rev. B* **1997**, *55*, 15701.
[29] G. Bartsch, M. Gerbracht, D. R. Yakovlev, J. H. Blokland, P. C. M. Christianen, E. A. Zhukov, A. B. Dzyubenko, G. Karczewski, T. Wojtowicz, J. Kossut, J. C. Maan, M. Bayer, *Phys. Rev. B* **2011**, *83*, 235317.
[30] G. Garcia-Arellano, K. Boujdaria, M. Chamarro, C. Testelin, *Phys. Rev. B* **2022**, *106*, 165201.
[31] L. M. Roth, B. Lax, S. Zwerdling, *Phys. Rev.* **1959**, *114*, 90.
[32] M. Altarelli, N. O. Lipari, *Phys. Rev. B* **1973**, *7*, 3798.
[33] K. Cho, S. Suga, W. Dreybrodt, F. Willmann, *Phys. Rev. B* **1975**, *11*, 1512.
[34] H. Venghaus, *Phys. Rev. B* **1979**, *19*, 3071.
[35] G. Wang, L. Bouet, M. M. Glazov, T. Amand, E. L. Ivchenko, E. Palleau, X. Marie, B. Urbaszek, *2D Mater.* **2015**, *2*, 034002.
[36] T. Wozniak, P. E. Faria-Junior, G. Seifert, A. Chaves, J. Kunstmann, *Phys. Rev. B* **2020**, *101*, 235408.
[37] T. Deilmann, P. Krüger, M. Rohlfing, *Phys. Rev. Lett.* **2020**, *124*, 226402.
[38] V. M. Goldschmidt, *Naturwissenschaften* **1926**, *14*, 477.
[39] D. N. Dirin, I. Cherniukh, S. Yakunin, Y. Shynkarenko, M. V. Kovalenko, *Chemistry of Materials* **2016**, *28*, 8470.
[40] J. Höcker, F. Brust, M. Armer, V. Dyakonov, *Cryst. Eng. Comm.* **2021**, *23*, 2202.
[41] A. V. Stier, K. M. McCreary, B. T. Jonker, J. Kono, S. A. Crooker, *Nat. Commun.* **2016**, *7*, 10643.
[42] H. G. Häfele, in *Landau Level Spectroscopy*, (Eds.: G. Landwehr, E. I. Rashba), Elsevier, Amsterdam, **1991**, pp. 208–275.